Dynamic Response of Shell-like Hyperbolic Paraboloid (HP) Concrete Beams: Comparing Experimental Modal Analysis (EMA) with Numerical

Dynamic Response of Shell-like Hyperbolic Paraboloid (HP) Concrete Beams: Comparing Experimental Modal Analysis (EMA) with Numerical Finite Element Analysis (FEA)

Alexander Sehlström

WSP, Göteborg, Sweden

David Selse, Erik Wigh, Rasmus Rempling

Chalmers University of Technology, Göteborg, Sweden

Contact: alexander.sehlstrom@wsp.com

Abstract

This paper examines the dynamic response of shell-like hyperbolic paraboloid (HP) shaped concrete beams. It compares experimental modal analysis (EMA) results with finite element analysis (FEA) and Euler-Bernoulli beam model results. It presents a case study involving a 3×0,6-meter steel reinforced, non-prestressed HP concrete specimen. EMA based on a roving hammer test provides the first six eigenfrequencies and mode shapes along with modal damping ratios, which are evaluated against numerical results.

Keywords: hyperbolic paraboloid; concrete shell; experimental modal analysis; finite element analysis; slabs; bridges.

1 Introduction

Hyperbolic paraboloid (HP) shell structures resist load primarily through membrane action, enabling thinner cross-sections with reduced material usage and environmental impact of up to 70% compared to bending-active slabs [1]. The doubly ruled geometry of HP shells enables reinforcement and prestressing with exclusively straight elements, lowering construction effort compared to other shell typologies. Beginning in the 1950s, long-span prefabricated prestressed HP elements, e.g., the Silberkuhl system, was used for roofing [2], however few or no applications has been built over the last few decades.

Recent interest in prestressed HP elements has led to studies on their structural optimization [3], building acoustics [4], methods for multi-objective optimization of structural and acoustic properties [5], and sandwich panel applications [6]. However, further research is needed to understand their dynamic behaviour in floor and bridge deck applications, which remains less explored compared to prismatic beams and slabs.

This paper examines the dynamic response of a 3×0,6-meter steel reinforced, non-prestressed HP concrete specimen. While real applications generally require longer spans and thicker covers or non-corrosive reinforcement, the specimen is a lab-scale model shaped by practical constraints.

2 Specimen characteristics

The specimen design is based on earlier works by Arlinger [1]. Figure 1 illustrates the middle surface of the specimen with length $\ell = 3$ m, width $w = 0{,}6$ m, and rise $r = 0{,}2$ m. The surface is offset equally upward and downward to get a 45 mm thick element which is fitted with 60 mm thick abutments extending 38 mm below the lowest point of the bottom surface. Figure 2 illustrates how it is reinforced with Ø6 mm K500C-T hook-ended straight bars in the two ruler directions spaced at ~60 mm, hook-ended bent bars in the transverse direction spaced at 150 mm, and bars following the perimeter, resulting in a reinforcement content ratio of 2,1%.

The specimen was cast on 25 June 2024 using a C25/30 concrete mix prepared with CEM II/B-M (S-LL) cement. It was concreted manually without mechanical vibration. It remained outdoors for curing until 20 February 2025 when the formwork was removed and the specimen moved indoors. Five mechanically vibrated standard-sized cubes were cast and cured along the specimen. Table 1 lists the resulting concrete parameters obtained from compressive strength testing of three of the cubes.

Photogrammetry was used to generate a digital 3D model of the specimen. Based on the test cube density, the volume of the scanned geometry, and known reinforcement quantities, the specimen weight was estimated to 258 kg, conforming well with weight measurements using a scale.

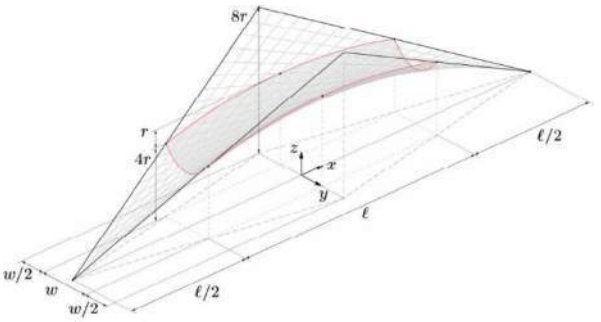

Figure 1. Element middle surface HP geometry.

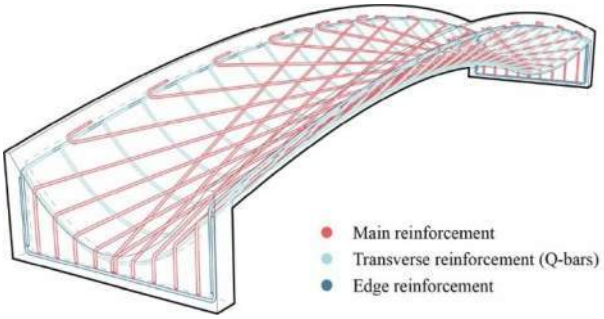

Figure 2. Element reinforcement.

3 Experimental modal analysis

The experimental modal analysis (EMA) was done to obtain the first six eigenfrequencies and mode shapes along with modal damping ratios.

3.1 Experimental setup

The EMA was based on a roving hammer single-input multiple-output (SIMO) setup.

3.1.1 Boundary conditions: air springs

Figure 3 shows the two Firestone model 116-1 air springs placed under each abutment to achieve as-free-as-possible boundary conditions without

Figure 3. Specimen with two air springs under each of its abutments.

Table 1. Concrete parameters obtained from three compressive strength cube tests.

f_{cm} [MPa]	f_{ck} [MPa]	f_{ctm} [MPa]	E_{cm} [GPa]	G_F [Nm/m²]	G_c [Nm/m²]	ε_{cu1} [‰]	ν [-]	ρ_c [kg/m³] [1]	ρ_{rc} [kg/m³] [2]
42,7	34,7	3,2	28,0	143	35750	3,5	0,2	2363	2476

[1] Plain concrete, [2] Assuming a 2,1% reinforcement content ratio.

suspending it, which was not possible. The air spring stiffness was evaluated at different internal pressures, indicating a linear correlation and good coherence with manufacturer data sheets.

3.1.2 Transducers: hammers & accelerometers

Two different PCB Piezotronics impact hammers were used. The useful frequency range of the larger 1,1 kg medium soft-tip hammer (PCB 086D20) was 0 Hz–280 Hz while for the smaller 0,16 kg hard steel tip hammer (PCB 086B03) it was 0 Hz–1000 Hz.

To measure the response, accelerometers were mounted on the prototype element using hot glue: two triaxial PCB TLD356A16 accelerometers with a sensitivity of 100 mV/g, two uniaxial PCB 352B accelerometers with a sensitivity of 1000 mV/g, and three uniaxial PCB 352C33 accelerometers with a sensitivity of 100 mV/g. Accelerometers were calibrated prior to installation using a Brüel & Kjær type 4294 calibration exciter.

3.1.3 Measurement grid

A 5-by-21-point grid with rectangles of approximate size 140×152 mm was marked on the top surface. The spatial coordinates of the points were retrieved from the photogrammetry texture map and the surface unit normal at these points computed to construct a reference model in DewesoftX, which was used to perform the experimental modal analysis. For each node, a local coordinate system was defined such that the local x- and y-axes aligned with the global and the local z-axis with the surface unit normal. Figure 4 illustrates the meshing.

3.2 Experimental procedure

A Dewesoft Sirius data acquisition (DAQ) system recorded and processed signals from the hammer and accelerometers. In addition, the DewesoftX software with its Modal Analysis Package, including signal processing, transfer function estimators, coherence plots, mode indicator function plots, averaging of hits, double hit detection, and curve fitting tools was used to extract modal parameters.

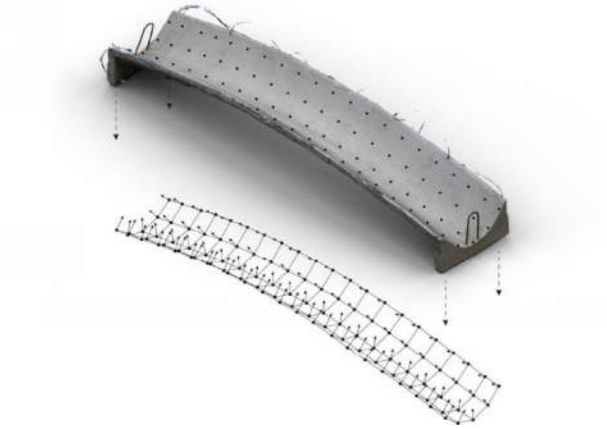

Figure 4. Coordinates of the marked points were extracted using photogrammetry scan which, along with their corresponding surface unit normal, defines the EMA gird.

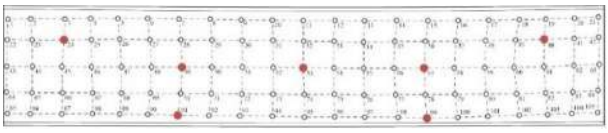

Figure 5. Red nodes indicate accelerometer locations for configuration C1 on the top surface.

Two accelerometer configurations were used: C1 had all seven accelerometers (position according to Figure 5) measuring acceleration normal to the surface, while C2 included one uniaxial and two triaxial accelerometers, with a separate channel allocated to each coordinate axis of the triaxial sensors. C2 allowed clearer identification of rigid body modes than C1.

The specimen was excited six times at each measurement grid node with the hammer, and results were averaged to minimise noise. Trigger and double hit detection thresholds ensured data quality, with thresholds set at 1000 N and 70 N, respectively, for the larger hammer and 200 N and 70 N, respectively, for the smaller hammer. Impacts were spaced in time to allow all vibrations to dissipate before the next excitation.

Transducer signals were sampled at 2000 Hz with 1024 spectral lines, giving a frequency resolution of 0,977 Hz (for positive frequencies) over a period of 1,02 s. Dynamic effects outside this window were excluded. Exponential windows with a 1% decay rate were applied to promote signal decay within the sampling period, assuming light damping. Anti-

aliasing infinite impulse (IIR) filters were applied to all signals.

3.2.1 Preliminary testing

Preliminary tests were conducted with both hammers to assess accelerometer locations, capture mode shapes and corresponding frequence, and impact-output coherence, resulting in these key observations:

- Six clear and distinguishable mode shapes were identified below 220 Hz. A seventh mode appeared near 300 Hz, though it was excluded as it exhibited poor definition and coherence.
- Three clear rigid body modes were observed: translation in the z-direction and rotations about the x- and y-axes, respectively. The remaining three rigid body modes were less distinct.
- Both hammers showed almost identical first six resonance frequencies, indicating linear element behaviour and minimal impact from input force magnitude.
- The largest rigid body mode exhibited a frequency ratio of less than 1:5 compared to the first flexible mode, suggesting the boundary conditions can be considered relatively free.
- The measurement grid was fine enough to capture and distinguish between mode shapes, and no refinement was deemed necessary.

For further testing, the larger hammer was selected because it demonstrated greater consistency and repeatability between strikes compared to the smaller hammer.

3.2.2 Air spring stiffness influence

The air spring air pressure influence was assessed by comparing the damped natural frequencies, modal damping ratios, and mode shapes across three configurations: 10 psi, 20 psi, and 40 psi. This corresponds to approximate spring stiffnesses of 55 N/mm, 90 N/mm, and 140 N/mm, respectively. Table 2 summarizes the results for the highest rigid body mode and the first six flexural modes.

As expected, the rigid body modes shifted with varying support stiffness. Ideally, rigid body modes should be as close to 0 Hz as possible to minimise their influence on the flexible modes. In this case, however, the measured damped natural frequencies, especially the higher-order ones, appeared to be largely unaffected by the frequency at which rigid body modes occurred.

Table 2. Damped eigenfrequencies, f [Hz], and modal damping ratios, ξ [%], at different air spring pressure levels.

P[1]	10 psi		20 psi		40 psi	
M[2]	f	ξ	f	ξ	f	ξ
HRB[3]	6,58	–	10,3	–	12,15	–
1	50,55	0.55	50,97	0,58	52,00	0,56
2	71,45	0.52	71,63	0,55	72,48	0,52
3	77,69	0.46	77,75	0,48	78,42	0,46
4	139,80	0.50	138,07	0,71	139,74	0,49
5	188,84	0.90	188,10	0,86	189,75	0,56
6	212,68	0.76	213,00	0,83	212,81	0,47

[1] Pressure level, [2] Mode, [3] Highest rigid body mode.

The first three modes exhibited comparable damping ratios at all pressure levels, indicating minimal boundary condition impact. At 10 psi and 20 psi, damping increased gradually with mode number. In contrast, this pattern was not observed at 40 psi, where modes 4–6 exhibited lower damping values than those in the lower-pressure scenarios. These results indicate that higher modes respond to variations in support stiffness, with boundary interactions contributing more to damping under softer support conditions.

Six mode shapes for each pressure configuration were compared using the modal assurance criterion (MAC), producing three 6×6 MAC matrices: 10 vs 20, 20 vs 30, and 30 vs 10 psi. Ideally, a MAC matrix should be the identity matrix. The most notable deviation occurs in the comparison between 10 psi and 40 psi, and 20 psi and 40 psi, particularly for mode 2 and mode 4 (bending modes), where the MAC drops to 0,96. Although still high, this suggests that there is some influence from the boundary conditions. In contrast, the comparison between 10 psi and 20 psi yields MAC values consistently at or above

0,99 for all modes, demonstrating excellent modal consistency.

The test results show that internal air pressures of 10 psi or 20 psi more closely simulate free boundary conditions compared to 40 psi. The 40-psi configuration increased stiffness, which influenced measured frequencies, mode shapes, and damping ratios. The frequency of the highest rigid body mode should be no more than 20% of the first flexural mode [7]. Although the 20-psi configuration did not fully meet this requirement, it was used for further testing based on the cushion manufacturer's recommendation to maintain a pressure of at least 20 psi during operation.

3.2.3 Modal parameter extraction

The final modal characteristics were determined using the larger hammer and 20 psi air springs.

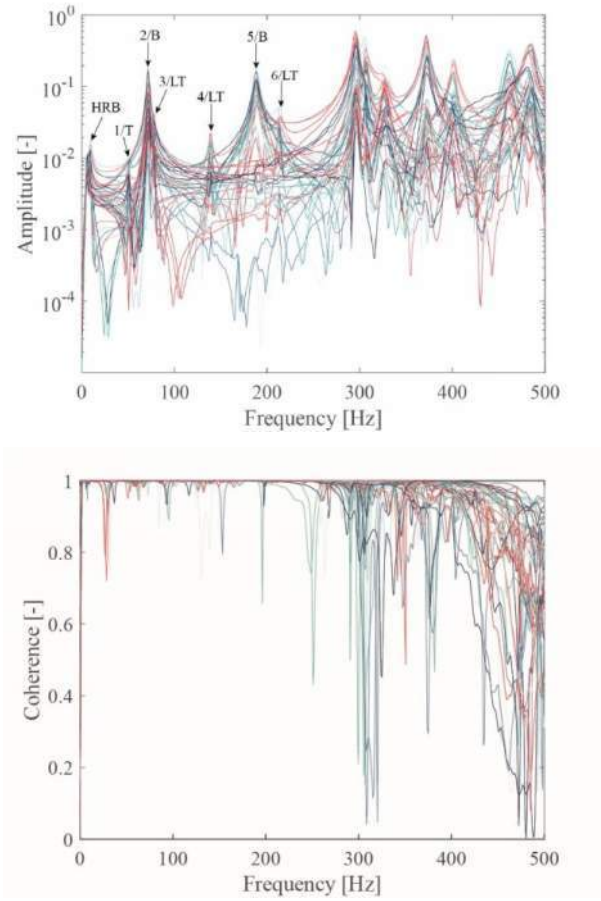

Figure 6. 50 arbitrary FRFs (top) and the corresponding coherence functions (bottom).

Figure 6 presents 50 estimated Frequency Response Functions (FRFs) and the corresponding coherence functions between input and output signals, showing strong coherence up to about 280 Hz, after which it declines noticeably. Coherence neared unity at resonance peaks below 280 Hz, matching the hammer's useful frequency range. Overlaid FRF functions exhibit modal peak alignment across all plots, i.e., they appeared at consistent frequencies independent of excitation intensity, indicating linear structural behaviour and validating the results for further analysis.

The damped natural frequencies ω_k and damping ratios ζ_k were obtained from DewesoftX using a least square complex frequency (LSCF) curve fitting approach [8]. Figure 7 includes a stabilisation chart (SC) and complex mode indicator function (CMIF) plot. The SC indicates that the estimated ω_k and ζ_k

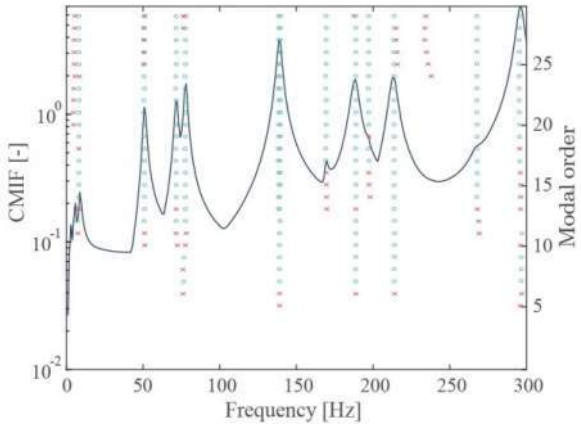

Figure 7. Stabilisation chart overlaid the CMIF plot.

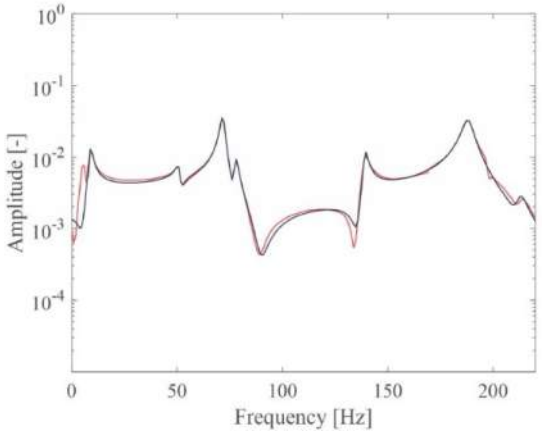

Figure 8. Synthesised FRF (blue) and original FRF (red) at node 57, from excitation at node 40.

vary by less than 1% and 5%, respectively. The modal order of the CMIF plot is 24, yielding stable poles for the six flexural modes of interest. The highest rigid body mode and the 7th mode were included as residual terms to improve the accuracy of the curve fitting for the 1st and 6th modes. Figure 7 validates that the identified poles correspond to the actual system resonances. A minor peak in the CMFI plot at 169 Hz suggests a local mode, excluded from further analysis.

Figure 8 compares the original FRF, measured at node 57 in response to excitation at node 40, with the synthesised FRF obtained from the modal model. The synthesised FRF closely follows the measured one, particularly at resonance peaks. This level of agreement was observed consistently across all 735 synthesised FRFs (7 accelerometer × 5×21 nodes), demonstrating that the modal model accurately represents the dynamics within the relevant frequency range.

4 Numerical modal analysis

Numerical modal analysis (NMA) was performed by modelling the specimen in ABAQUS/CAE. The purpose of the modelling and comparison to EMA results is to establish a methodology for future accurate NMA modelling of similar HP elements for which EMA is not available.

4.1 Sensitivity study

The sensitivity study aimed to find a suitable model for further analysis. Four models were considered: 1) 3D solid with reinforcement included explicitly, 2) 3D solid without reinforcement, 3) 2D shell with reinforcement including Rebar Layer in Abaqus, and 4) 2D shell without reinforcement. Free vibration behaviour was analysed under free boundary conditions without damping using the concrete parameters in Table 1. The following outlines the sensitivity study by [9].

4.1.1 Influence of reinforcement inclusion

Effective reinforced concrete density (ρ_{cr}) was applied for models without reinforcement to get the correct mass. No modification was made on the bending stiffness to compensate for the stiffness contribution of the excluded reinforcement.

Including reinforcement increased the stiffness of the models, particularly in bending modes, leading to higher eigenfrequencies. MAC plot comparison of mode shapes revealed that the mode shapes remained virtually identical regardless of reinforcement inclusion.

4.1.2 Influence of element type

Second-order elements were used, with and without reinforcement. Two element types were considered: 10-node tetrahedral and 20-node hexahedral for 3D models, and 6-node triangular and 8-node quadrilateral for 2D models. Element type had little influence on modal frequencies. Hexahedral and quadrilateral elements were used for their accuracy and better convergence.

Mesh sizes of 150, 100, 75, 50, 25, and 10 mm were analysed. An inverse relationship between mesh size and frequencies was observed. Eigenfrequencies consistently decreased as the mesh was refined. Eigenfrequencies converged for all configurations with mesh sizes of 75 mm or less, which was used for further analysis.

4.1.3 Influence of boundary conditions

The supporting air springs provide vertical stiffness through the cushion and horizontal stiffness via frictional contact. Vertical spring stiffnesses of 55, 90, and 140 N/mm, corresponding to 10, 20, and 40 psi, were investigated by examining the eigenfrequencies of the rigid body mode and the first six modal frequencies using model 1 (see § 4.1). The findings were in line with the EMA spring stiffness influence tests. When infinite horizontal stiffness was evaluated, significant changes in dynamic characteristics were observed. The prototype's in-plane restraint level was not further validated; instead, restraints were calibrated by aligning the rigid body modes of the numerical models with the experimental results.

4.2 Model calibration

Models 1 and 2 (see § 4.1) were calibrated to ensure their responses corresponded with

experimental results and to understand what factors limits coherence between EMA and NMA. The mass was matched to the measured value by adjusting the concrete density for both models. For Model 1, reinforcement density was further reduced to account for overlapping volumes in the finite element model. Concrete stiffness and Poisson's ratio were modified to minimize discrepancies with experimentally observed damped natural frequencies. Additionally, the support spring stiffnesses were iteratively refined so that the numerically calculated rigid body modes aligned with those experimentally recorded.

4.3 Final model setup

Figure 9 illustrates the final model setup used in the NMA.

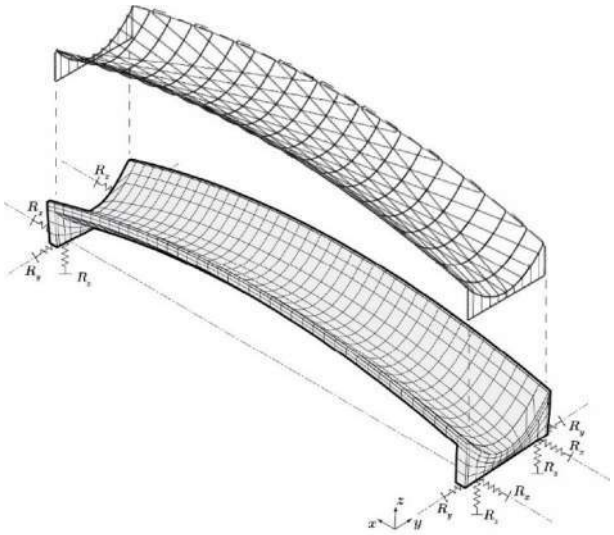

Figure 9. Final FE model 1 configuration with explicitly modelled reinforcement. In Model 2, the reinforcement stiffness is embedded in the concrete elements.

5 Results

Table 3 presents modal parameters from EMA and NMA from the first six modes and the highest rigid body mode. For EMA, it shows damped frequencies, damping ratios (corrected for artificial damping from the exponential window function), and the mode complexity factors (MCF). For NMA,

Table 3. Damped frequencies, damping ratios, and MCF from EMA LSCF curve fitting, and natural (undamped) frequency from NMA for the HP specimen.

M[1] / C[2]	EMA			NMA
	Freq.[4] [Hz]	Damping [%]	MCF [%]	Freq.[5] [Hz]
HRB[3]	10,3	–	–	10,6
1 / T	50,9	0,57	0,73	47,9
2 / B	71,6	0,56	1,02	75,9
3 / LT	77,7	0,49	1,10	79,6
4 / LT	138,4	0,76	1,03	138,6
5 / B	188,1	1,06	1,05	196,0
6 / LT	212,9	0,81	1,03	209,2

[1] Mode, [2] Characteristics (T=Torsion, B=Bending, LT=Lateral torsion), [3] Highest rigid body mode, [4] Damped, [5] Undamped.

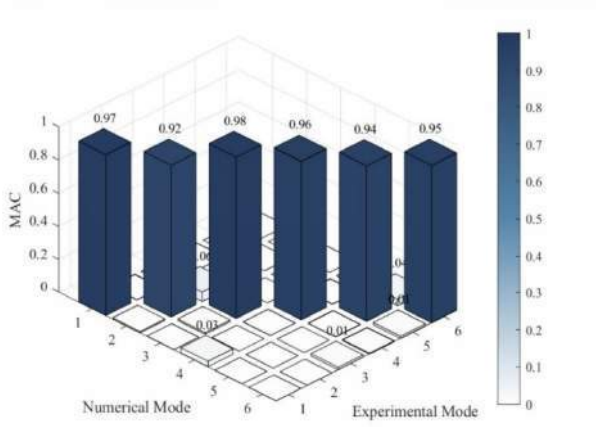

Figure 10. MAC comparison of EMA and NMA results.

it lists the natural frequency. Figure 10 compares the modes from the two methods in a MAC plot.

6 Conclusions

This paper examines the dynamic response of shell-like hyperbolic paraboloid-shaped concrete beams by comparing experimental modal analysis with finite element analysis results.

6.1 Experimental data quality

Damping ratios of uncracked concrete are typically 0,1%–1,0%, increasing with the presence of microcracks, pores, or other irregularities [10], thus, the EMA results indicate the specimen is likely undamaged. Low MCF indicates little damping and predominantly real and physical mode shapes, and its small imaginary component implies near-proportional damping, with points vibrating generally in phase. Low MCF also reflects good data quality, as high values often indicate noise or non-linearities.

6.2 EMA and NMA coherence

Comparing mode shapes from EMA and NMA yields high MAC values, indicating the numerical model captures the real behaviour well. This alignment supports the general validity of the modelling approach. However, several limitations and opportunities for improvement were identified.

Despite a strong correlation, NMA could not simultaneously replicate the bending and torsional behaviour observed in EMA, regardless of how the numerical models were calibrated. This suggests that the chosen NMA may not fully capture the real structural response seen in EMA. While fixing the mass and support spring stiffnesses and altering the concrete stiffness to minimize the mean error of the first six modes, no satisfactory solution was found; to minimize errors of bending modes, the E-module had to be decreased while increased to minimize errors of torsion modes.

It is thought that the reinforcement representation in the NMA contributes significantly to the observed discrepancy, and that the reinforcements contribution to directional stiffness and bending-torsion coupling currently is inadequately captured. Future work could explore more sophisticated modelling approaches, e.g., by introducing interface elements between bars to simulate mechanical interlocking of the reinforcement cage, better capturing its bending and torsional stiffness. However, the origin of this mismatch cannot be unambiguously attributed to reinforcement modelling alone. Conducting EMA on an unreinforced specimen would provide a critical reference case, enabling isolation of the structural response of the concrete body itself. If satisfactory agreement between EMA and NMA can be achieved for such a specimen, discrepancies observed in the reinforced specimen of this paper could be directly linked to reinforcement effects. Conducting EMA on a reinforcement cage alone could also provide further insight.

NMA relied on idealised geometry and material properties, whereas the specimen exhibited imperfections introduced during casting, including asymmetry, curvature deviations, and thickness variations, making stiffness distribution deviate from idealisation, likely affecting coupled modes. To minimize sources of error, future studies could improve accuracy by basing numerical models on scanned geometries, thereby incorporating otherwise neglected geometric irregularities. Alternatively, introducing stochastic or controlled perturbations in the NMA by varying stiffness and mass of individual finite elements to replicate voids and material inconsistencies.

7 Acknowledgements

We salute Ju-Hung Pai, Johan Jonsson, Claes Fredö, and Penka Dinkova for their profound interest, sharing their expertise, and generous support while we learnt EMA. Thanks to Jens Ahrens, Astrid Pieringer, and Krister Larsson at Chalmers Dept. of Applied Acoustics for providing measurement equipment, and to Peter Folkow and Håkan Johansson at Chalmers Dept. of Applied Mechanics for laboratory access.

8 References

[1] Arlinger E. Design and evaluation of doubly-curved shell-like concrete slab elements: Pre-stressed structurally optimized elements and their potential to reduce the climate impact. *MSc thesis*. Chalmers University of Technology, 2023.

[2] Scheffler T. Development and application of precast hyperboloid shells in East and West Germany from the 1950s to the 1980s. In: *Proceedings of IASS Annual Symposia*. International Association for Shell and Spatial Structures (IASS), 2017.

[3] Osman-Letelier JP, Lehrecke J, Schlaich M. Structural optimization of prestressed concrete shells with ruled surface geometry. In: Lázaro C, Bletzinger K-U, Oñate E (eds). *Form and Force 2019*. International Centre for Numerical Methods in Engineering (CIMNE): Barcelona, Spain, 2019, pp 2622–2629.

[4] Eddin AE, Merz P, Dombrowski M, Heidemann L, Reinhold S, Loutfi J et al. Building acoustic analysis of doubly curved beam-like shell floors made of CFRP prestressed concrete and its integration into an interdisciplinary optimisation tool. In: Block P, Boller G, DeWolf C, Pauli J, Kaufmann W (eds). *IASS 2024 Symposium - Redefining the Art of Structural Design*. IASS, 2024.

[5] Loutfi J, Dombrowski M, Merz P, Eddin AE, Schlaich M. Interdisciplinary optimisation tool for doubly curved beam-like shell floors made of CFRP prestressed concrete. In: Block P, Boller G, DeWolf C, Pauli J, Kaufmann W (eds). *IASS 2024 Symposium - Redefining the Art of Structural Design*. IASS, 2024.

[6] Stark A, Classen M, Knorrek C, Camps B, Hegger J. Sandwich panels with folded plate and doubly curved UHPFRC facings. *Structural Concrete* 2018; **19**: 1851–1861.

[7] Ewins DJ. Modal testing: theory, practice and application. Baldock: Research Studies Press; 2000.

[8] Guillaume P, Verboven P, Vanlanduit S, Van der Auweraer H, Peeters B. A poly-reference implementation of the least-squares complex frequency-domain estimator. In: Proceedings of IMAC-XXI: Conference & Exposition on Structural Dynamics; 2003 Feb 3-6; Kissimmee, Florida, USA. Bethel, CT: Society for Experimental Mechanics; 2003.

[9] Selse D, Wigh E. Dynamic and static response of beam-like hyperbolic paraboloid concrete elements: A numerical, analytical, and experimental study. *MSc thesis*. Chalmers University of Technology, 2025.

[10] Gidrão G, Krahl P, Bosse R, Silvestro L, Scoczynski Ribeiro R, Terezinha dos Santos Lima G, Carrazedo R. Internal damping ratio of normal- and high-strength concrete considering mechanical damage evolution. Buildings. 2024;14.